

Coordinated 1996 HST and IRTF Imaging of Neptune and Triton

I. Observations, Navigation, and Differential Deconvolution¹

L. A. Sromovsky² and P. M. Fry

Space Science and Engineering Center, University of Wisconsin, Madison, Wisconsin 53706

E-mail: larry.sromovsky@ssec.wisc.edu

K. H. Baines²

Jet Propulsion Laboratory, California Institute of Technology, Pasadena, California 91109

S. S. Limaye

Space Science and Engineering Center, University of Wisconsin, Madison, Wisconsin 53706

G. S. Orton²

Jet Propulsion Laboratory, California Institute of Technology, Pasadena, California 91109

and

T. E. Dowling

Comparative Planetology Laboratory, University of Louisville, Louisville, Kentucky 40292

Received July 15, 1999; revised October 17, 2000

On 13–14 August 1996, we carried out the first coordinated contemporaneous imaging of Neptune, using the Hubble Space Telescope (HST) Wide Field Planetary Camera 2 and the NASA Infrared Telescope Facility (IRTF) NSFCAM InSb camera to obtain high spatial resolution absolutely calibrated imagery at wavelengths from 0.2 to 2.5 μm . We used nine HST orbits to provide unique dynamical coverage of a single rotation of Neptune. During three orbits we obtained virtually simultaneous groundbased images. These data provide an extended range of wavelengths that sample the Rayleigh scattering regime, both strong and weak methane bands, and strong near-infrared hydrogen collision-induced opacity bands, from which strong constraints can be obtained on the properties of Neptune's cloud features. We developed very precise navigation techniques, which were required to achieve colocation of the observations from these different observatories. Technique advances include compensating for limb profile distortions by bright cloud

features in HST images and dealing with a nearly invisible limb in the near-IR groundbased images. We achieved RMS center-finding accuracy of 0.003''–0.006'' (0.05–0.1 pixels) for HST navigations. To obtain the subpixel navigation accuracy of the groundbased images, we determined NSFCAM pixel scale versus wavelength and as a function of location on the detector, establishing a distortion correction equation for NSFCAM imaging. This permitted use of a navigation method based on offsetting from Triton, with which we achieved IRTF center-finding accuracy of 0.02'' (0.1 pixel) RMS, and 0.2–0.3 pixels absolute. We developed a novel differential deconvolution method for significantly reducing deconvolution artifacts within the planetary disk and improving convergence properties for planetary cloud features, resulting in by far the most detailed groundbased images of Neptune yet obtained without speckle imaging or adaptive optics. © 2001 Academic Press

Key Words: Neptune; Neptune, atmosphere; Triton; infrared observations; data reduction techniques.

¹ Based on observations made with the NASA/ESA Hubble Space Telescope, and on observations obtained from the data archive at the Space Telescope Science Institute. STScI is operated by the Association of Universities for Research in Astronomy, Inc. under NASA Contract NAS 5-26555.

² Visiting Astronomer at the Infrared Telescope Facility, which is operated by the University of Hawaii under contract to the National Aeronautics and Space Administration.

1. INTRODUCTION

We present the results of a campaign to simultaneously observe Neptune from Hubble Space Telescope (HST) and the NASA Infrared Telescope Facility (IRTF) located on the summit of Mauna Kea, Hawaii. This produced the first simultaneous

high-resolution absolutely calibrated imaging of Neptune over the highly diagnostic 0.2–2.4 μm spectral range. The HST Wide Field Planetary Camera 2 (WFPC2) observations provide high spatial resolution imaging for exploring horizontal and vertical cloud structure at CCD wavelengths (0.2–1.1 μm), while observations with the IRTF NSFCAM InSb array camera at near-IR wavelengths (1.1–2.5 μm) provide access to strong methane and hydrogen absorption bands that allow a greater discrimination of high altitude vertical cloud structure.

This paper (I) describes our observing strategy, the basic characteristics of the observations, the special methods used for geometric correction and image navigation, the methods of deconvolution that we applied to the groundbased images, and the effects of deconvolution on geometry and photometry. To unambiguously identify the same cloud features in both groundbased and HST data sets, significant advances had to be made in geometric correction and navigation techniques. Advances in HST image navigation were also needed to permit accurate circulation measurements over the relatively short time spans needed to obtain high confidence in cloud feature identity. To obtain maximal scientific return from both HST and groundbased observations, subpixel navigation is absolutely essential and achievable with the techniques described in subsequent sections.

Paper II (Sromovsky *et al.* 2001a, this issue) describes our photometric analysis of the HST and IRTF data sets, for both Neptune and Triton, focusing on disk-integrated results and the interpretation of spectral and temporal variations in terms of cloud structure. Paper III (Sromovsky *et al.* 2001b, this issue) describes the atmospheric circulation results we obtained from our 1996 observations and new results obtained from 1994 and 1995 HST archived observations, as well as the first-order results on the vertical cloud structure of discrete features.

2. OBSERVATIONS

2.1. 1996 HST WFPC2 Observations

On 13 August 1996 we used the WFPC2 to image one rotation of Neptune using nine orbits of imaging spanning a range of 11 successive HST orbits and covering a period of 16.6 h. This is longer than the 16.11-h rotation period of Neptune’s interior (Warwick *et al.* 1989), but is shorter than the nearly 20 h it takes equatorial cloud features to complete a full rotation. During each 90-min HST orbit, Neptune was visible for about 45 min, during which we were able to obtain between six and seven images. Image times, filters, and exposures are provided in Table I.

The temporal sampling of the observations was chosen with three main objectives in mind: (1) complete longitudinal coverage to ensure detection of all significant cloud features, (2) multiple views of features at time intervals that allow measurement of wind speed and dynamical changes without ambiguities about feature identification, and (3) views at different illumination and observing angles for vertical cloud structure analysis. With these objectives and a limited number of HST orbits available to us, we chose to sample one rotation of Neptune much more intensively

TABLE I
1996 HST WFPC2 Observations of Neptune

Filename	UT Date DD/MM/YY	UT time HH:MM:SS	Filter	Expo- sure (s)	ORIEN- TAT (°)	Relative orbit
pu3fc0101	13/08/96	08:33:16	F467M	40	121.27	1
pu3fc0102	13/08/96	08:36:16	F673N	160	121.27	1
pu3fc0103	13/08/96	08:45:16	FQCH4N-D	500	121.27	1
pu3fc0104	13/08/96	09:00:16	F850LP	20	121.27	1
pu3fc0105	13/08/96	09:04:16	FQCH4N-B	300	121.27	1
pu3fc0106	13/08/96	09:13:16	F631N	70	121.27	1
pu3fc0107	13/08/96	10:03:16	FQCH4N-D	400	121.27	2
pu3fc0108	13/08/96	10:15:16	F850LP	20	121.27	2
pu3fc0109	13/08/96	10:18:16	F467M	40	121.27	2
pu3fc010a	13/08/96	10:21:16	F673N	160	121.27	2
pu3fc010b	13/08/96	10:26:16	F255W	200	121.27	2
pu3fc010c	13/08/96	10:37:16	FQCH4N-D	400	121.27	2
pu3fc010d	13/08/96	11:38:16	F467M	40	121.27	3
pu3fc010e	13/08/96	11:41:16	F673N	160	121.27	3
pu3fc010g	13/08/96	12:04:16	F850LP	20	121.27	3
pu3fc010h	13/08/96	12:07:16	F336W	100	121.27	3
pu3fc010i	13/08/96	12:11:16	F588N	70	121.27	3
pu3fc010j	13/08/96	12:15:16	F410M	100	121.27	3
pu3fc0201	13/08/96	15:00:16	F467M	40	125.27	5
pu3fc0202	13/08/96	15:03:16	F673N	160	125.27	5
pu3fc0203	13/08/96	15:11:16	FQCH4N-D	500	125.27	5
pu3fc0204	13/08/96	15:26:16	F850LP	20	125.27	5
pu3fc0205	13/08/96	15:30:16	FQCH4N-B	300	125.27	5
pu3fc0206	13/08/96	15:39:16	F631N	70	125.27	5
pu3fc0207	13/08/96	16:29:16	FQCH4N-D	400	125.27	6
pu3fc0208	13/08/96	16:42:16	F850LP	20	125.27	6
pu3fc0209	13/08/96	16:45:16	F467M	40	125.27	6
pu3fc020a	13/08/96	16:48:16	F673N	160	125.27	6
pu3fc020b	13/08/96	16:53:16	F255W	200	125.27	6
pu3fc020c	13/08/96	17:03:16	FQCH4N-D	400	125.27	6
pu3fc020d	13/08/96	18:04:16	F467M	40	125.27	7
pu3fc020e	13/08/96	18:07:16	F673N	160	125.27	7
pu3fc020f	13/08/96	18:16:16	FQCH4N-D	500	125.27	7
pu3fc020g	13/08/96	18:31:16	F850LP	20	125.27	7
pu3fc020h	13/08/96	18:34:16	F336W	100	125.27	7
pu3fc020i	13/08/96	18:38:16	F588N	70	125.27	7
pu3fc020j	13/08/96	18:42:16	F410M	100	125.27	7
pu3fc0301	13/08/96	21:26:16	F467M	40	125.26	9
pu3fc0302	13/08/96	21:29:16	F673N	160	125.26	9
pu3fc0303	13/08/96	21:38:16	FQCH4N-D	500	125.26	9
pu3fc0304	13/08/96	21:52:16	F850LP	20	125.26	9
pu3fc0305	13/08/96	21:56:16	FQCH4N-B	300	125.26	9
pu3fc0306	13/08/96	22:05:16	F631N	70	125.26	9
pu3fc0307	13/08/96	22:55:16	FQCH4N-D	400	125.26	10
pu3fc0308	13/08/96	23:07:16	F850LP	20	125.26	10
pu3fc0309	13/08/96	23:10:16	F467M	40	125.26	10
pu3fc030a	13/08/96	23:13:16	F673N	160	125.26	10
pu3fc030b	13/08/96	23:18:16	F255W	200	125.26	10
pu3fc030c	13/08/96	23:29:16	FQCH4N-D	400	125.26	10
pu3fc030d	14/08/96	00:30:16	F467M	40	125.26	11
pu3fc030e	14/08/96	00:33:16	F673N	160	125.26	11
pu3fc030f	14/08/96	00:42:16	FQCH4N-D	500	125.26	11
pu3fc030g	14/08/96	00:57:16	F850LP	20	125.26	11
pu3fc030h	14/08/96	01:00:16	F336W	100	125.26	11
pu3fc030i	14/08/96	01:04:16	F588N	70	125.26	11
pu3fc030j	14/08/96	01:08:16	F410M	100	125.26	11

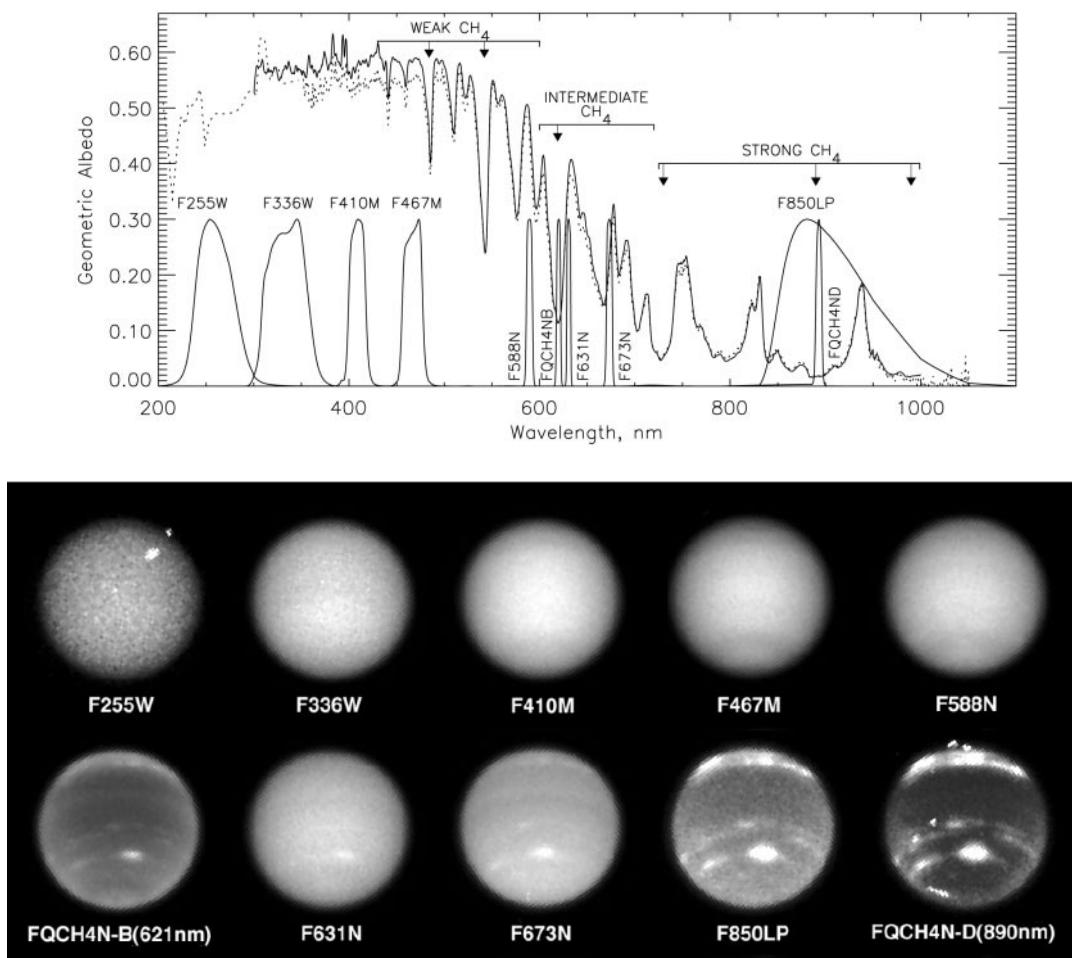


FIG. 1. (Upper) WFPC2 filter system response functions, normalized to a unit maximum and scaled by the factor 0.3, compared to Neptune's geometric albedo spectrum, the dashed version from Neff *et al.* (1984), adjusted to account for differences in Neptune radius and a 3% bias error (Neff *et al.* 1985), and the solid line from Karkoschka (1994). The UV continuum region (dashed) is from Baines and Smith (1990) based on IUE observations by Caldwell *et al.* (1981). (Lower) Representative WFPC2 images of Neptune illustrating characteristics for each of the filters used in 1996 observations. The top row of images are from orbits 10 and 11 (start times 23:18, 25:00, 25:08, 24:30, 25:04) and the bottom images are from orbit 9 (start times 21:56, 22:05, 21:29, 21:52, 21:38). In F255W and FQCH4N-D images, the bright features with sharp edges are due to cosmic rays.

than any previous HST Neptune program. Although longer time intervals between images can lead to higher wind accuracy for stable cloud tracers, shorter time intervals provide much better longitude coverage, better coverage of feature evolution, and the possibility of tracking small features that do not live long enough to be seen after a full rotation of Neptune. The longitude sampling is most demanding at high northern latitudes because Neptune's north pole is tipped away from the Earth (in 1996 the sub-Earth latitude was 27.5°S planetographic) and because one of the most important targets (the GDS near 32°N) is affected by limb darkening at the best observing wavelength and by low inherent contrast. Even with our frequent sampling in 1996, we only captured the GDS itself in one image. At lower latitudes and especially at southern latitudes, our sampling results in multiple views of the same feature on the same rotation of Neptune. The exact sampling for each feature we tracked is given in Paper II.

The filters referenced in Table I are defined by the system response plots in Fig. 1, where they are shown overlaid on plots of Neptune's geometric albedo spectrum. At wavelengths beyond 500 nm this spectrum becomes increasingly dominated by methane absorption bands, which have value in estimating the vertical cloud structure (e.g., Hammel *et al.* 1989, Baines and Smith 1990, Baines and Hammel 1994). The detailed photometric characteristics of the filters are provided in Paper II. Filters were selected to maximize contrast of Neptune's cloud features, to characterize changes in the vertical structure of the features, and to provide good correlation with ground observations and Voyager imaging data. Characteristic Neptune images for the filters we used are provided in the lower panel of Fig. 1.

Four filters that we chose to carry the main burden of tracking dynamical changes were used on every orbit. The F467M filter was selected to provide the best imaging of dark features. This filter is similar to the Voyager blue filter ($0.43\text{--}0.53\ \mu\text{m}$), which

gave the greatest contrast for the Great Dark Spot (Smith *et al.* 1989). The new dark spot near 32°N was seen in an F467M HST image (Hammel *et al.* 1995), and what we believe is the same feature is also visible (barely) in the F467M image shown in Fig. 1. Other dark features, including southern and northern dark bands, are also visible in this image. All these features are relatively subtle in the raw images and become much more obvious when limb darkening is removed (see Paper III). Note that images at nearby wavelengths, using F410M and F588N filters, provide much reduced contrast for these features.

The F673N filter is in a region of relatively low CH_4 absorption and less affected by Rayleigh scattering than the blue region of the spectrum. It thus provides views similar to the Voyager orange filter ($0.54\text{--}0.64\ \mu\text{m}$) (cf. Smith *et al.* 1989), showing mid level (such as the Scooter) and higher bright cloud features as well as showing subtle banded structure quite well, including a dark narrow band near the equator that does not appear in the $0.619\text{-}\mu\text{m}$ methane-band image. The FQCH4N-D filter covering the $0.89\text{-}\mu\text{m}$ methane band provides very high contrast for bright cloud features and good views of the limb. It was at $0.89\ \mu\text{m}$ that discrete cloud features on Neptune were first imaged in 1979 by Smith and Reitsema (1982). The F850LP filter provides a shorter exposure view of essentially the same cloud features seen at $0.89\ \mu\text{m}$, but with much greater signal/noise ratios.

Among the less frequently sampled filters, the $0.619\text{-}\mu\text{m}$ filter, which can't probe deeper than ~ 3 bars (Paper III), is insensitive to some of the lower cloud features and subtle zonal bands but gives enhanced views of the upper level haze layer that produces a limb-brightened disk. This and the $0.89\text{-}\mu\text{m}$ filter allow us to constrain the altitudes of the cloud/haze layers in

the upper atmosphere where the vertical distribution of methane vapor is known (Baines and Hammel 1994). The $0.631\text{-}\mu\text{m}$ filter (F631N) provides a relatively clean continuum reference for the $0.619\text{-}\mu\text{m}$ band. Short wave bands that can discriminate vertical structure by varying amounts of Rayleigh scattering are provided by F255W, F336W, F410M, and F588N. The UV filter F255W, which has never revealed any discrete cloud features, was only used during every third orbit of observation, while the latter three filters were alternated with FQCH4N-B during the remaining orbits. While no discrete features were seen in the F336W images, they do show a small hemispheric brightness asymmetry of unknown origin (see Fig. 1). A more detailed characterization of the vertical sampling of the HST filters is provided in Paper III.

2.2. Overview of 1994–1996 HST Observations

Our analysis also makes use of recent HST observations during 1994–1996, most of which are described by Hammel and Lockwood (1997) who provide a detailed log for 10–11 and 18–19 October 1994, 1–2 November 1994, 1–2 September 1995, 22, 24 November 1995, and 6 March 1996. They also provide figures displaying every image in their program. Observations by J. Trauger and associates in 27–29 June 1994 are described by Crisp *et al.* (1994). The HST images prior to August 1996 do not provide closely spaced observations over a single rotation, but instead provide a longer view of Neptune's variation, which is treated in Paper III. An overview of the temporal and spectral sampling of these various imaging observations is provided in Fig. 2, where we plot times at which

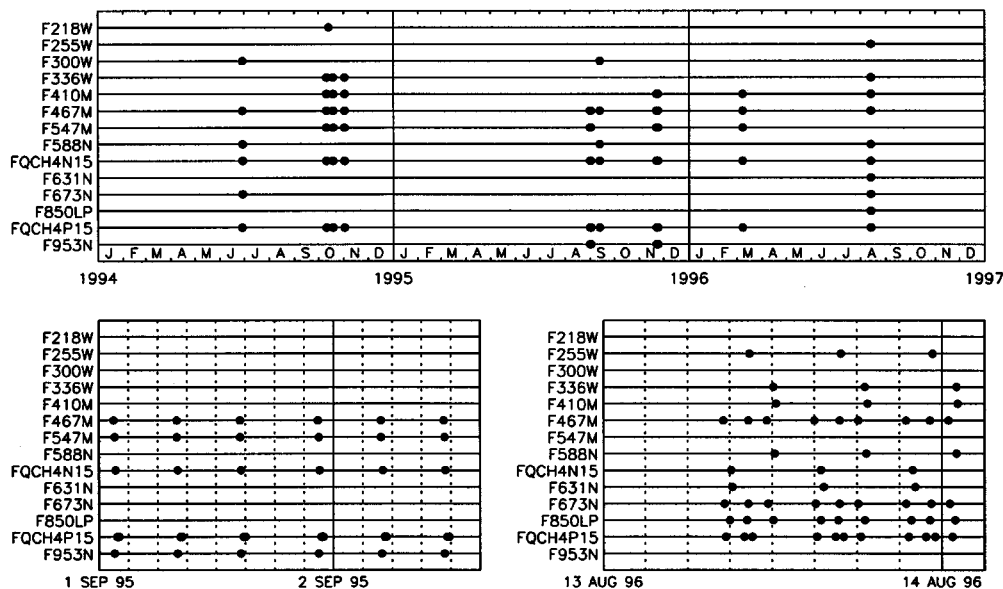


FIG. 2. Temporal and spectral sampling of 1994–1996 HST Neptune imaging data sets. The top panel provides a three-year overview. The lower two panels provide more detailed views of 1–2 September 1995 and 13–14 August 1996. Vertical solid lines show year or day boundaries; vertical dotted lines are at every 3 hours. Date labels are centered at 00:00 UT on the day labeled. The 10–11 October, 18–19 October, and 1–2 November 1994 periods each provides only three sample times over one Neptune rotation.

each image is made in each filter. The top panel provides a 3-year view, with the lower panels providing higher resolution views of periods best suited for making cloud motion measurements: 1–2 September 1995 and 13–14 August 1996. Note the unusually frequent temporal sampling and the large number of filter used in our 1996 program in comparison to other data sets.

2.3. IRTF NSFCAM Observations

Our groundbased observations of Neptune were made with the IRTF facility instrument NSFCAM, an InSb infrared array camera providing selectable pixel scales and a wide variety of broadband and narrowband filters (Legget and Denault 1996). We chose a nominal image scale of $0.148''/\text{pixel}$ to capture both Neptune and Triton in the same image so that we could use Triton for three purposes: (1) as a positional reference point, (2) as a PSF reference for deconvolution, and (3) as a photometric reference that simultaneously samples nearly the same terrestrial atmospheric path as the Neptune measurements.

We acquired IRTF NSFCAM images on 13 and 14 August 1996, using J, H, K, and Spencer 1.73- μm filters, as well as the NSFCAM Circular Variable interference Filter (CVF) at 1.59 μm and within the 2.1- μm H_2 CIA band. Figure 3 dis-

plays the transmission curves for these filters over a sample spectrum of Neptune obtained by Fink and Larson (1979). The CVF filters are labeled by central wavelength. Their bandwidths are about 2% (Legget and Denault 1996). Most of the features in the Neptune spectrum are due to methane bands. An exception is in the range 2.0–2.1 μm where hydrogen absorption dominates, but where the Fink and Larsen spectrum is poorly defined. The rather regular modulations seen beyond 2 μm are at the noise level, and are not seen in more recent preliminary spectra of much greater relative precision (Sromovsky *et al.* 1998), nor in model calculations discussed in Paper II. Because Neptune's atmosphere is so dark within these various absorption bands, high-altitude clouds are seen with very high contrast at these wavelengths.

Characteristic images of Neptune for each NSFCAM filter are provided in the lower panel of Fig. 3, both in raw and deconvolved forms. These images were made about 16 h before the top row of HST images shown in the lower panel of Fig. 1. The prominent bright cloud feature near the top of the IRTF images is the companion to the northern GDS feature visible (very faintly) in the F467M HST image. The near-IR images all provide high-contrast views of the discrete bright features, but

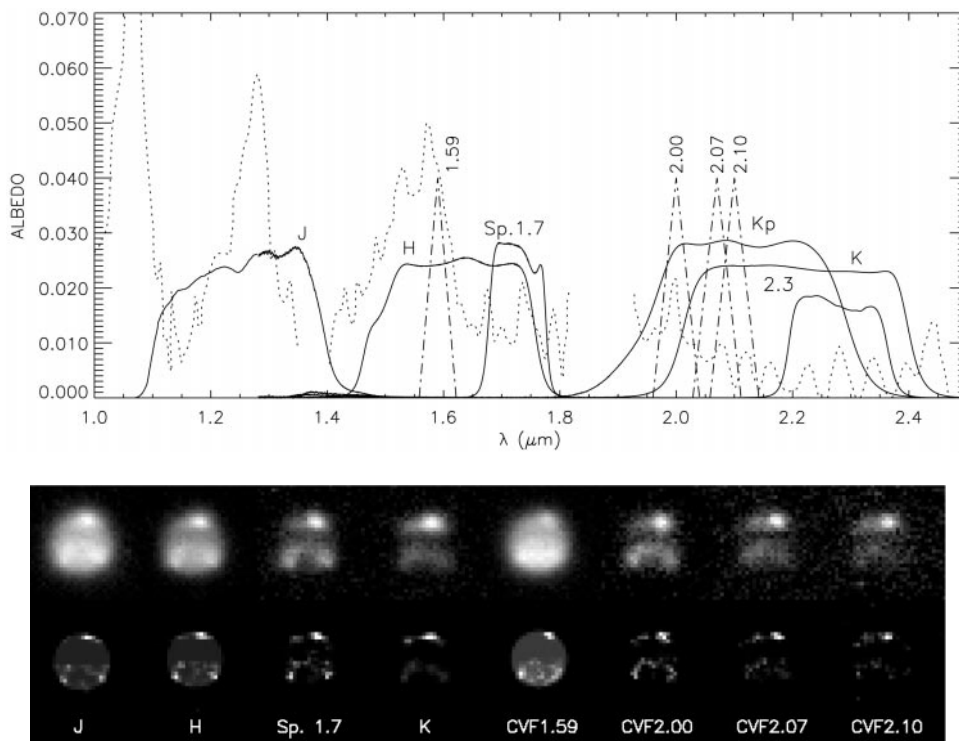


FIG. 3. (Upper) NSFCAM filter transmission functions, scaled by a factor 0.03 for comparison with Neptune's geometric albedo spectrum (Fink and Larson 1979); broadband transmissions include the effects of blockers, but do not account for detector quantum efficiency. Circular variable interference filter response functions are schematically indicated by triangular response functions with a FWHM of 2% and a peak arbitrarily set to 0.04. (Lower) Representative NSFCAM images of Neptune from 13 August 1996 (at UT start times of 7:51, 7:59, 8:15, 8:04, 8:25, 8:31, 8:35, and 8:39 from left to right). Exposures were $0.5 \text{ s} \times \text{coadds}$ of 10, 10, 40, and 80 for J–K, and $5 \text{ s} \times \text{coadds}$ of 10, 20, 20, and 20 for CVF 1.59–2.1. Raw images are shown on the top row and deconvolutions on the bottom row. Differential deconvolution was used for J, H, Sp. 1.7, and CVF 1.59 images (see text).

TABLE II
13 August 1996 (UT) IRTF Observation Summary

Filename(s)	Target/purpose/seeing	Filters	Air mass	Start time (UT)	HST orbit
flat001–016.a	dome/flats	All		04:53:30.0	
nep0157–0194.a, b	Neptune/focus	J	1.57	06:40:46.5	
nep0195–272.a, b	Neptune/1.2''	J, H, K, Sp. 1.7, K	1.50	06:55:40.6	
nep0273–356.a, b	Neptune/0.69''	J, H, K, Sp. 1.7, J	1.35	07:51:19.6	
nep0357–372.a, b	Neptune/0.63''–0.45''	CVF 1.59, 2.0, 2.07, 2.1	1.32	08:23:11.7	1
nep0377–378.a, b	Neptune/0.47''	J	1.31	08:50:50.4	1
ura0383–0410.a, b	Uranus/scale	J, H, K, Sp. 1.7	1.31	08:56:29.1	1
ura0413–0414.a, b	Uranus/scale	CVF 1.59, 2.00	1.31	09:16:05.3	
nep0563–581.a, b	Neptune	J	1.40	09:54:30.6	
nep0582–589.a, b	Neptune/0.63''	H	1.41	10:01:55.2	2
nep0590–593.a, b	Neptune	K	1.43	10:05:47.0	2
nep0594–597.a, b	Neptune	Sp. 1.7	1.44	10:13:44.2	2
ukirt34.0598–603.a, b	UKIRT FS34 ^a /cal.	J	1.34	10:21:19.2	2
ukirt34.0604–611.a, b	UKIRT FS34/cal.	J, H, Sp. 1.7, K	1.35	10:25:20.4	2
ukirt34.0612–619.a, b	UKIRT FS34/cal.	J, H, Sp. 1.7, K	1.36	10:32:35.6	2
gaql0620–631.a, b	γ Aql/cal.	CVF 1.59, 2.0	1.18	10:43:26.8	
gaql0632–639.a, b	γ Aql/cal.	CVF 1.59, 2.0, 2.07, 2.1	1.20	10:53:18.7	
gaql0640–641.a, b	γ Aql/cal.	CVF 2.00	1.21	10:55:30.7	
gaql0642–649.a, b	γ Aql/cal.	CVF 1.59, 2.0, 2.07, 2.1	1.21	10:56:58.3	
nep0650–0673.a, b	Neptune/focus/0.8''	J	1.65	11:01:17.9	
nep0674–0679.a, b	Neptune/0.8''	J	1.72	11:10:06.3	
nep0680–0685.a, b	Neptune	H	1.73	11:13:44.7	
nep0686–0689.a, b	Neptune	K	1.75	11:16:07.8	
nep0690–0693.a, b	Neptune	Sp. 1.7	1.78	11:20:50.4	
nep.0772–781.a, b	Neptune	J	2.00	11:43:27.9	3
nep.0782–787.a, b	Neptune, 1.37''	H	2.05	11:48:42.1	3
nep.0788–789.a, b	Neptune	K	2.07	11:51:04.1	3
nep.0790–793.a, b	Neptune	Sp. 1.7	2.15	11:57:56.9	3
ukirt34..0794–801.a, b	UKIRT FS34/cal.	J, H, Sp. 1.7, K	1.69	12:02:19.1	3
ukirt34..0802–809.a, b	UKIRT FS34/cal.	J, H, Sp. 1.7, K	1.74	12:09:12.2	3
gaql0810–817.a, b	γ Aql/cal.	CVF 1.59, 2.0, 2.07, 2.1	1.70	12:20:25.7	
gaql0818–825.a, b	γ Aql/cal.	CVF 1.59, 2.0, 2.07, 2.1	1.73	12:23:14.3	

^a Faint star No. 34 on the UKIRT target list.

only J, H, and CVF 1.59 filters transmit much reflected light from Neptune's disk. Not surprisingly, the CVF 1.59 filter, which samples only a spectral band of minimal methane absorption and can sense levels deeper than 20 bars in a clear atmosphere (Paper III), provides the brightest atmospheric disk. It is interesting that no new horizontal spatial structure is seen in these images. Comparing this to a K-band image, for which methane absorption blots out everything deeper than 1 bar (see Paper III), we see a reversal of contrast between several northern and southern cloud features, indicating that the southern features are at a lower effective altitude (as demonstrated in Paper III). This is further indicated in Fig. 3 by the relative dimming of the southern features with increasing H₂ absorption at wavelengths from 2.0 to 2.1 μ m.

The spatial resolution of the groundbased images in Fig. 1 was substantially improved from $\sim 0.5''$ to $\sim 0.15''$ – $0.25''$ using our differential deconvolution technique, which is described in Section 7.3. These images provide fairly typical examples of what can be expected using Triton as a PSF reference at the $0.148''$ /pixel image scale.

2.4. Observing Sequence

The IRTF observing sequence is summarized in Table II for 13 August 1996 and Table III for 14 August 1996. In these tables, the times are given for the start of the first image in the group named in the first column. The 13 August observations included about two hours of overlap with HST imaging during which we obtained essentially simultaneous observations, some with $0.5''$ seeing.

3. HST DATA PROCESSING

The Neptune images used in this analysis were calibrated by the Space Telescope Science Institute by the Routine Science Data Processing pipeline. This includes A/D correction, bias level correction, dark correction, and flat field correction as described in Chapter 26 of the HST Data Handbook (Voit 1997). Since the original calibration of the 1994 and 1995 data sets, a completely new generation of flats was delivered between late 1995 and 1996, and used for the 1996 data set. In the visible,

TABLE III
14 August 1996 (UT) IRTF Observation Summary

Filename(s)	Target/purpose/seeing	Filters	Air mass	Start time (UT)	Relative time
nep0059–70.a, b	Neptune/0.65''	J	1.39	07:28:49.4	22.926
nep0071–94.a, b	Neptune	H, Sp. 1.7, K	1.34	07:31:59.5	22.979
nep0095–121.a, b	Neptune	J, H, Sp. 1.7	1.34	07:55:23.6	23.369
nep0122–129.a, b	Neptune	CVF 1.59, 2.0, 2.07.2.1	1.32	08:14:25.1	23.686
nep0130–137.a, b	Neptune/0.58''	CVF 1.59, 2.0, 2.07.2.1	1.32	08:28:27.9	23.920
nep0140–165.a, b	Neptune/focus	J	1.31	08:43:24.1	24.169
ura0166–171.a, b	Uranus/scale	J	1.31	08:58:43.5	
ura0172–173.a, b	Uranus/scale	CVF 1.59	1.31	09:00:37.0	
ura0174–197.a, b	Uranus/scale	J, H, Sp. 1.7, K, J	1.31	09:03:12.3	
ura0263–265.a, b	Uranus/scale	J	1.31	09:33:13.7	
ura0266–273.a, b	Uranus/scale	CVF 1.59, 2.0, 2.07.2.1	1.31	09:34:12.6	
nep0274–301.a, b	Neptune/1.1''	J, H, Sp. 1.7, K	1.41	10:00:18.8	25.451
nep0302–321.a, b	Neptune	J	1.46	10:17:41.2	25.740
nep0322–345.a, b	Neptune/0.8''	J, H, Sp. 1.7, K	1.50	10:27:03.3	25.897
nep0346–369.a, b	Neptune	J, H, Sp. 1.7, K	1.57	10:41:35.1	26.139
nep0370–377.a, b	Neptune	CVF 1.59, 2.0, 2.07.2.1	1.64	10:55:29.0	26.370
nep0378–410.a, b	Neptune	J, H, J, H, Sp. 1.7, K	1.75	11:09:44.6	26.608
ukirt320411–428.a, b	UKIRT FS34 ^a /Cal.	J, H, Sp. 1.7, K	1.55	11:28:32.1	
gaql0429–444.a, b	γ Aql/Cal.	CVF 1.59, 2.0, 2.07, 2.1	1.47	11:47:00.3	
nep0449–470.a, b	Neptune	J, H, Sp. 1.7	2.20	11:55:28.0	27.370
nep0471–492.a, b	Neptune	J, H, Sp. 1.7, K	2.36	12:02:21.9	27.485
ura0493–496.a, b	Uranus/scale	J, CVF 2.14	2.11	12:15:21.3	
gaql0499–508.a, b	γ Aql/Cal.	CVF 1.59, 2.0, 2.07, 2.1, 2.14	1.83	12:28:47.0	
gaql0515–522.a, b	γ Aql/Cal.	CVF 1.59, 2.0, 2.07, 2.1	1.84	12:34:50.5	

^a Faint star No. 34 on the UKIRT target list.

the new flats differ from the old flats by 1% or less over the vast majority of the chip, but by up to 8% in the outer 50 pixels of the chip at all wavelengths. Longward of 850 nm, differences up to 1.5% are seen over the main part of the chip, and shortward of 300 nm, differences are less than 3% over most of the chip. Neither Neptune nor Triton calibrations require significant corrections for the revised flats. Neptune is usually observed near the center of the PC chip, and although Triton is observed closer to the edge of the chip, in no case do we make use of observations with Triton within 50 pixels of the edge and in most cases the image is greater than 100 pixels distant.

4. NAVIGATION OF HST IMAGES

HST image navigation is simpler than IRTF navigation for two reasons: (1) all the HST images are at wavelengths for which Neptune has a well-defined limb that can be used to locate its center to high accuracy; and (2) the orientation of the camera is provided by STScI calculations that are ultimately confirmed by guide star observations. In most cases, when Triton is contained within the image, we are able to verify image scale and orientation by measuring the vector from Neptune to Triton, and comparing that with ephemeris computations.

The HST central image scale is $0.04554 \pm 0.00001''/\text{pixel}$, but varies with position within the camera field of view as a result of distortion (Biretta *et al.* 1996). In using observations of Neptune and Triton to verify pixel scale and orientation it is

necessary to make corrections of up to 1 pixel, to account for this distortion. The correction equations are provided in the instrument handbook (Biretta *et al.* 1996), and also can be obtained with the STSDAS routine METRIC. Distortion is not significant within a region the size of Neptune's disk, usually about 50 pixels in diameter, and near the center of the FOV. One pixel width at the center of Neptune corresponds to physical distance of about 1000 km.

The position of Neptune's center in image coordinates is the key navigation parameter that we need to measure for each image. The algorithm we used is illustrated in Fig. 4. First, the image is clipped to eliminate bright interior cloud features; this is done by setting any pixel exceeding the median brightness equal to the median brightness. Second, a gradient image is computed using the maximum of gradients in x and y directions. The third step is to locate two absolute gradient maxima along all rows within about half a planet radius of the center, and another set of paired maxima along all columns within about half a planet radius of the center. Next, the paired left and right coordinates of the gradient maxima are averaged to produce a midpoint estimate for each row, and a straight line is fit to the midpoints versus row number. Similarly, the paired top and bottom gradient maxima are averaged to produce a set of up–down central points that are then used to determine a best-fit straight line, with column number (x coordinate) as the dependent variable. For most images, the last step is to locate the intersection of these two lines, which is taken as the initial best estimate of the planet

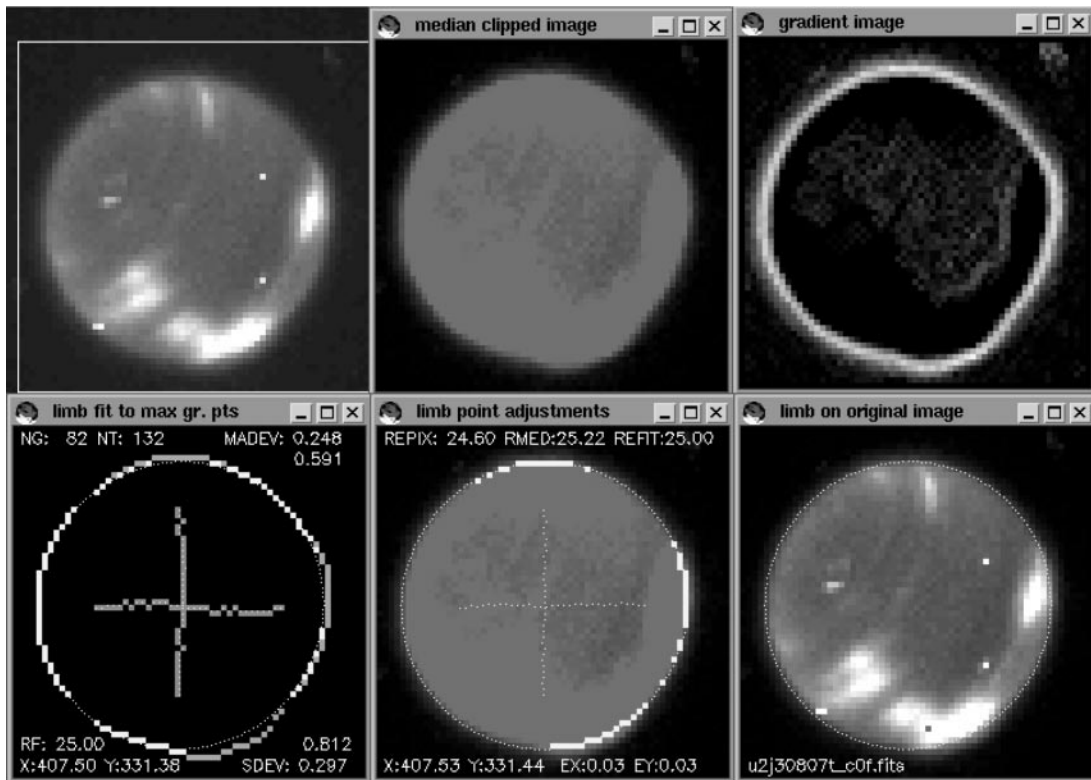


FIG. 4. Finding coordinates of Neptune’s center in HST images. The unaltered HST image is shown in the upper left, a median-clipped image in the upper center, a gradient image in the upper right, and an image of maximum gradient points in the lower left, with limb points within acceptable distance of a fit limb shown brighter than those rejected. The modified limb points and revised intersection fits are shown in the remaining two images. Note the significant limb distortion produced by bright cloud features near the limb. This is an extreme example.

center. This is a valid estimate for the center of any elliptical figure, and has the virtue of not depending on any knowledge of ellipse orientation or exact size.

For images in which discrete cloud features near the limb greatly exceed the background brightness (or median brightness), the limb becomes distorted by energy distributed across the limb by the wings of the point-spread function, the most extreme example of which is illustrated in Fig. 4. We deal with this problem, which is only significant for the FQCH4N-D filter ($0.89\ \mu\text{m}$), by fitting an elliptical curve to the part of Neptune’s limb that is not so distorted and replace the limb points that extend a critical distance beyond the fitted limb with the fitted limb points. We then proceed as before, except for increasing the uncertainty estimate by reducing the statistical count of limb points. We estimate that planet centers for the FQCH4N-D images have errors of about $0.05\text{--}0.1$ pixels, depending on the distribution of cloud features, with the remaining images having center coordinate errors in the range $0.04\text{--}0.05$ pixels. These error estimates are further validated in Appendix B.

5. IRTF IMAGE PREPROCESSING

Offsets were removed by subtracting dark frames taken with the same filter and exposure, but at an angular offset of typically

$10''$. Our procedure was to expose pairs of images with Neptune and Triton placed within the initial frame so that they also appear within the shifted frame, thus providing two independent dark-subtracted images of our targets. The dark subtraction resulted in a sky average within 0.5 DN of zero, and thus is significantly smaller than other error sources. NSFCAM responsivity variations over the detector face, typically 3% over small scales and 25% over large scales, were removed by division of filter-dependent flat-field images. Flats were obtained by pointing the telescope at the inside of the dome and taking the difference of two exposures, one with dome lights on and one without lights. Each flat is normalized by the average value of the central $196\text{--}196$ -pixel subimage, which samples most of the frame while avoiding edge artifacts. The normalizing factor is, in any case, arbitrary, as long as the same flat is used for all images using the same filter.

Linearity measurements made on 12 August 1996 did not show a significant effect at DN levels below 1000. Thus we did not make linearity corrections for any of the Neptune images, as their DN values per image are well below 1000.

6. NAVIGATION OF IRTF IMAGES

Establishing the relationship between image pixel coordinates and latitude and longitude coordinates on the planet’s cloud

top surface requires three distinct kinds of information: (1) the observing geometry obtained from ephemerides, including the range and orientation of the planet; (2) instrument characteristics, which include the image scale and distortion; and (3) image-specific information, including the camera orientation and location of the planet center within the image.

In most cases we obtained Ephemeris information from the NAIF kernel files using the SPICE Toolkit N0049 (Acton, 1996). We also used the online Horizon program provided by the Solar Systems Dynamics Group at JPL (Giorgini *et al.* 1998). The two sources, which we generally found to agree within 1 milliarcsecond, both rely on the same kernel files: `ura031.bsp` (for Uranus and Satellites, Ephemeris Code URA031) and `nep016.5.bsp` (for Neptune and Triton, Ephemeris Code NEP016.5). In converting image coordinates to planetary coordinates we follow NAIF in using IAU values of 24,764 and 24,341 km for Neptune's equatorial and polar radii at the 1-bar level (Davies *et al.* 1992).

The usual method for locating the planet center is to fit a predicted limb profile to the observed limb, but for most IRTF filters, a well-defined Neptune atmospheric limb is not present in the images. Methane absorption makes most of Neptune's visible disk extremely dark, so that discrete high-altitude cloud features provide most of the reflected sunlight. Lacking a well-defined limb to define Neptune's center, we developed an alternative method that makes use of Triton as a position reference. We measured Triton's location in image coordinates and then offset by the distance and in the direction defined by ephemeris vectors. This requires a precise knowledge of image scale and image orientation. Given that Triton is typically 16'' from Neptune, the typical offset distance is 108 pixels. The NSFCAM lens turret was set to the nominal 0.148''/pixel mode to ensure that Neptune and Triton could simultaneously fit within the 256-pixel \times 256-pixel NSFCAM image.

The accuracy of the offset navigation method is limited by four independent error sources: (1) uncertainty in the image x coordinate of Triton; (2) uncertainty in the y coordinate of Triton; (3) uncertainty in the image scale; and (4) uncertainty in image y -axis orientation relative to celestial north. If we aim to make navigation errors a negligible contribution to positional uncertainties, we must keep the combined navigation error significantly less than the 0.289-pixel uncertainty due to pixel quantization errors. If we aim for a combined RMS navigation error of 0.1 pixels in both x and y coordinates, this places very tight bounds on the contributing uncertainties. Because (3) and (4) contribute in orthogonal directions, as do (1) and (2), they can each be apportioned an effective resulting standard deviation of $0.1/\sqrt{2}$ pixels. To meet this budget the image scale would need to be known to within about 0.07%, and the orientation within 0.66 milliradians (about 0.04°). In addition, we would have to be able to locate Triton within 0.07 pixels. While these are tough requirements, we have found that they are feasible to attain in many cases.

6.1. Image Scale and Orientation Angle

Image scale (angular size of pixels) and image orientation relative to celestial north were determined from measurements of uranian satellite positions and comparing them to ephemeris positions. We used NAIF ephemeris file URA031, the most accurate available for the 22-Oct-85 through 5-Jan-2000 time period (Jacobson *et al.* 1991). The 1- σ uncertainties in position relative to the planetary system barycenter for the uranian satellites is 200 km or about 0.015'' (Jacobson, personal communication; Jacobson *et al.* 1991). On 13 August 1996, the Umbriel–Ariel separation was about 22'', so that ephemeris uncertainty contributes about 0.1% to the scale uncertainty. Given that the pixel scale is consistent within better than 0.1%, it appears that for a series of images taken within an hour or so, the ephemeris error must be considered a bias, and applied after random errors are averaged.

All scale determinations were obtained from Ariel and Umbriel, using 15 images in five different filters. We first measured the coordinates of the satellites using two dimensional Gaussian fits, then corrected the coordinates for distortion, as described in Appendix A, and determined the distance between them in corrected image pixels. We then determined the Ariel–Umbriel position angle relative to the image y axis, from which we computed the counterclockwise angle from celestial north to the camera Y axis. For 13 and 14 August 1996 we found no orientation dependence on filter and average orientation angles of $0.686 \pm 0.008^\circ$ and $0.664 \pm 0.005^\circ$ respectively, which agree well within our required accuracy of 0.04° . The scale results are shown in Table IV and Fig. 5, where we find a significant variation of image scale with imaging filter. The uncertainty estimates are based on Monte Carlo simulations of the fitting process (Appendix B). Typically we are able to locate Ariel and Umbriel within 0.015–0.02 pixels.

In Fig. 5 we also compare the average scales derived from the satellite measurements on 13 August 1996 with those derived using paired star observations. The latter results were obtained by measuring interstellar angular separations at a variety of wavelengths, then normalizing to the corresponding measurements in K -filtered images. Using a scale factor determined by χ^2 minimization, we fit this relative function to the absolute scale values derived from the uranian satellites. The relative results (Table IV and Fig. 5) confirm the smaller scale values for J, H, and Spencer 1.7 filters, and provide additional information for estimating scales for CVF wavelengths of 1.59 and 2.1 μm , for which no satellite observations are available. For the CVF filters, we could discern no clear scale dependence on filter, and thus adopted a single scale value equal to that of the K filter, which is consistent also with the relatively accurate determination for the 2.00- μm filter.

The adopted scale values are summarized in Table IV and shown as circles in Fig. 5. The variability of these results from one image to the next is smaller than might be expected from the 1- σ ephemeris uncertainty. In fact, measurements of image

TABLE IV
Measured and Adopted NSFCAM Image Scales in Arcseconds/Pixel

Filter	From star pairs ^{a,b,c}	From 13 Aug 96 Uranian satellites ^c	From 14 Aug 96 Uranian satellites ^c	Adopted values ^d
J + Blocker	0.1474 ± 0.0002	0.1460 ± 0.0001		0.1470 ± 0.0002
J w/o Blocker			0.14747 ± 0.00005	0.1475 ± 0.0002
H	0.1479 ± 0.0001	0.1474 ± 0.0001	0.14731 ± 0.00002	0.1475 ± 0.0002
CVF 1.59	0.1475 ± 0.0002			0.1479 ± 0.0002
Sp. 1.7	0.1486 ± 0.0002	0.1471 ± 0.0001	0.14708 ± 0.00004	0.1471 ± 0.0002
CVF 2.00	0.1479 ± 0.0006	0.1479 ± 0.0002		0.1479 ± 0.0002
K	0.1478 ± 0.0002	0.1479 ± 0.0001	0.14791 ± 0.00004	0.1479 ± 0.0002
CVF 2.07	0.1477 ± 0.0004			0.1479 ± 0.0002
CVF 2.10	0.1481 ± 0.0003			0.1479 ± 0.0002

^a For scale factor of $0.1478 \pm 0.0001''/\text{pixel}$.

^b Uncertainties listed here are in addition to the above scale factor uncertainty.

^c Includes distortion corrections, but not ephemeris errors.

^d Includes ephemeris errors.

scales on 14 August 96, not used in formulating the adopted values (except for the J w/o blocker value), serve to confirm those values with very high accuracy (see Table IV). These results are also consistent with the Baines *et al.* (1998) value of $0.1478 \pm 0.0010''/\text{pixel}$, although our values are at least five times more precise, and thus are able to clearly resolve the filter dependencies.

Possible changes in scale associated with focus variations that occur during an observing run were investigated using 14 August 96 J-filtered images taken during focus adjustment. These images contained five stars in addition to Neptune and Triton. We measured distances between stars in each image and found that the variations with respect to focus were essentially random variations of about the magnitude expected from our un-

certainty estimates, and generally were well within 0.1% of the mean. There was no discernible trend indicating a dependence on focus, at least within the range that might be experienced in a night of observing.

The effect of differential atmospheric refraction on pixel scale, based on Allen (1964), scaled by a factor of 0.6 to account for the reduced atmospheric mass above 14,000 ft, evaluated for high-quality observations near 1.4 air masses, is only 0.035% and ignorable.

6.2. Offsetting from Triton

Procedures. We first deconvolved the images to be navigated using Triton's image as the PSF reference, which put the deconvolved Triton peak at the center of the pixel closest to the PSF peak. The central time of the exposure was used to determine angular offsets in right ascension and declination using the NAIF toolkit and ephemeris files already noted. Triton's position was measured in the image to subpixel accuracy, then corrected to the position it would have in an undistorted image of the central pixel scale appropriate to the filter used. Using the known image orientation and pixel scale, the angular offsets were converted to pixel offsets in the undistorted image. Finally, the distortion was applied to these coordinates to obtain the predicted center of Neptune in the distorted image.

Verification of accuracy. Offsetting accuracy can be partially verified by comparison with HST imagery, which is done in the next section. Two other methods are also available for checking offset navigation accuracy. First, we can make use of a reasonably well-defined limb in the deconvolved J and 1.59- μm images to do center finding based on limb fitting, which can then be compared with center locations derived from offset navigation. Second, we can use self-consistency of images taken nearby in time as a measure of relative accuracy of the system. Particularly demanding comparisons come from the

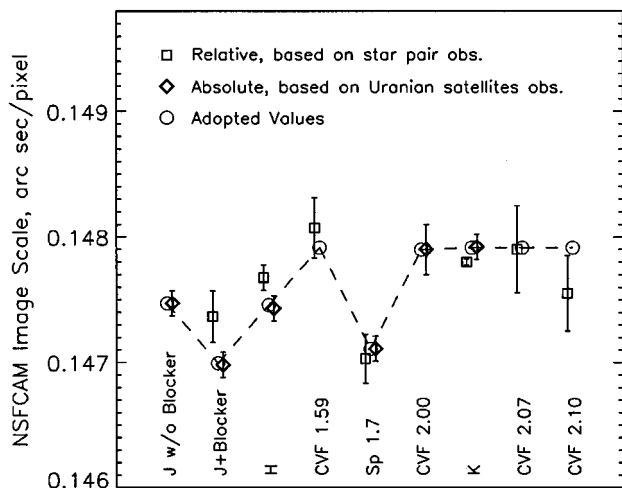


FIG. 5. IRTF NSFCAM image scale vs filter, from uranian satellite observations (diamonds), from scaled star-pair relative observations (squares), and the adopted values from Table IV (open circles connected by dashed line). The various symbols are horizontally offset slightly for clarity.

a–b pair images. While close together in time, they are obtained in directions that are $10''$ – $20''$ apart, putting both Neptune and Triton on different parts of the imaging array, and thus requiring different distortion corrections. In a limited set of limb-fitting comparisons we found center-finding differences of about 0.1–0.2 pixels. Consistency within about 0.1 pixels in both x and y coordinates was obtained in defining the location of bright features in a–b pairs relative to Triton using cross-correlation (see Appendix A). The consistency comparison in Section 7.4 for 15 closely spaced J-filter navigations and deconvolutions indicates feature centroid stability of 0.1 pixels RMS, and for the more localized cloud features, even peak pixel locations are consistent within 0.2–0.3 pixels RMS.

7. DECONVOLUTION

Because Triton provides a local and simultaneous recording of the point spread function during each exposure of Neptune, it has been possible to use deconvolution to significantly improve the resolution of most of our groundbased images. Based on measurements of deconvolved star profiles we were often able to improve the effective seeing by about a factor of 3, from initial values of $0.75''$ – $0.5''$ to about $0.25''$ – $0.15''$. In the following we describe the basic deconvolution techniques used, their limitations, and their effects on photometry. We also describe a novel technique for differential deconvolution that avoids introduction of artifacts in planetary disks.

7.1. Basic Techniques

We used the Space Telescope Science Data Analysis System (STSDAS; STSI 1998) implementation of the Lucy–Richardson deconvolution algorithm (Richardson 1972, Lucy 1974). An overview of the characteristics of the Richardson–Lucy (RL) algorithm and improvements to it is provided by White (1993). In its original form, the algorithm converges to the maximum likelihood solution for Poisson noise statistics using the following rather simple iteration procedure. Denoting $P(i | j)$ as the fraction of light from true location j that gets scattered into pixel i , which defines the point spread function (PSF), the noiseless blurred image can be written as

$$I(i) = \sum_j P(i | j) O(j), \quad (1)$$

where O is the unblurred object. The RL algorithm takes the n th estimate for the object image and improves it using the iteration equation

$$O_{n+1}(j) = O(j)_n \frac{\sum_i P(i | j) \frac{D(i)}{I(i)_n}}{\sum_i P(i | j)}, \quad (2)$$

where $D(i)$ is the observed image, and $I(i)_n$ is the n th estimate of the blurred image, given by substituting O_n into the right-hand side of Eq. (1).

The algorithm does have some serious drawbacks, however. To fit small noise bumps in a blurred image it can produce large peaks and surrounding valleys in the unblurred image. In an image of stars against a dark sky this noise amplification is limited by the requirement that the image be positive, so that once the image surrounding a bright pixel is pushed to 0, there is no further noise amplification. But in regions with a nonzero background, often seen in planetary disks, the attempt to fit noise fluctuations leads to a speckling of the smooth background, with speckle amplitudes that grow with iteration number. Read noise, which does not follow Poisson statistics, is in effect treated as a real characteristic of the observed object and can lead to significant anomalies in the image solution.

The STSDAS algorithm can reduce the impact of these problems by approximately accounting for read noise within the context of the inversion algorithm, which is done by replacing the ratio $D(i)/I(i)_n$ in Eq. (2) with $(D(i) + C)/(I(i)_n + C)$, where $C = R^2/K$, R is the read noise in electrons, and K is the number of electrons per DN. This leads to a variable rate of convergence in which bright objects are converged rapidly while dim objects converge slowly. This modification does not conserve flux locally and globally at each iteration, as does the standard RL iteration process.

7.2. Performance Characteristics

Two typical examples of how deconvolved image characteristics vary with RL iteration number are provided in Fig. 6. The left column contains a sequence of deconvolution steps for image 586 (13 Aug 96), made with an H filter and showing some background light from Neptune’s atmosphere. The right column is for image 596 (13 Aug 96), made with the Spencer $1.73\text{-}\mu\text{m}$ filter, and showing a very dark background with a few small bright cloud features. Also shown in each column are the images of Triton and a bright star. Despite the asymmetric appearance of the stellar image, emphasized by the enhancement chosen, the deconvolution has produced a highly sharpened stellar profile. From a FWHM of 3.76 pixels ($0.56''$), by 80 accelerated iterations it has improved to 0.94 pixels ($0.14''$), a factor of four improvement in linear resolution.

The integrated light from Neptune quickly attains a stable value that converges to about 1.08 times that for the input image. Triton’s integral converges at about 1.14 times the value obtained from the initial image. By the end of the iteration sequences, the contrast between bright and dark cloud regions has increased from 2 : 1 in both input images to 23 : 1 in the H image and to 69 : 1 in the Spencer $1.73\text{-}\mu\text{m}$ image. In the latter image, clouds are similar to stars against a dark sky, allowing large numbers of iterations without significant speckling. On the other hand, the H image shows objectionable noise speckles beyond 200 iterations. Because of increasing artifact amplitudes, there is not much improvement obtained beyond 80 iterations for the J, H, and 1.59 CVF images and 200 iterations for the Spencer $1.73\text{-}\mu\text{m}$ image. For the K-band images, 300 accelerated iterations seems

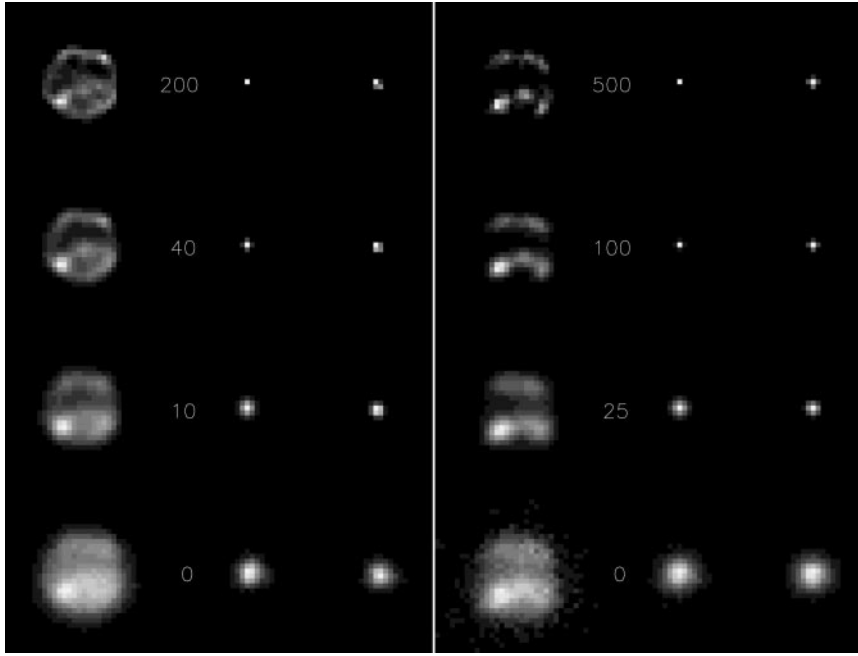


FIG. 6. Sample deconvolutions as a function of accelerated iteration number for image 586 (H) on the left, and 596 (Spencer 1.7) on the right. The images of Triton and a star are shown adjacent to Neptune.

to provide convergence without objectionable artifacts. A new deconvolution technique described in Section 7.3 permits 300 or more accelerated iterations for J and H, resulting in improved retrieval of discrete cloud feature details.

7.3. Differential Deconvolution

When we apply RL deconvolution to a synthetic image consisting of a blurred flat planetary disk, two problems result: (1) the sharp planetary edge causes a ringing in the deconvolved image, introducing concentric spurious rings that increase in spatial frequency with increasing iteration number, and (2) the elevated background level within the planetary disk allows large amplification of noise speckles, even though this is partially controlled by the improved algorithm that approximately accounts for read noise effects. The combined speckle amplification and annular pattern make it difficult to distinguish between real atmospheric feature and artifacts. However, these artifacts can be greatly reduced by applying what we call differential deconvolution.

The procedure for differential deconvolution is briefly as follows: (1) create a synthetic flat image of the planet that has the correct size and approximately the correct DN level of the atmospheric background that is free of discrete cloud features; (2) for the image to be processed, extract the subimage of Triton for use as a point spread function; (3) convolve the synthetic disk image with the Triton image to obtain an approximation of what Neptune's blurred image would be without the discrete cloud features; (4) subtract the convolved synthetic image from the observed image of Neptune, leaving what is primarily the

blurred image of the discrete cloud features; (4) deconvolve the difference image; and (5) add the deconvolved image to the initial synthetic image.

The mathematical basis for this process is that convolution is a linear operation. Using previously defined notation, we can thus decompose the unblurred object O into two components, an unblurred reference object O_{REF} and unblurred difference ΔO , such that the noiseless blurred image can be written as

$$\begin{aligned} I(i) &= \sum_j P(i | j) O(j) \\ &= \sum_j P(i | j) O_{\text{REF}}(j) + \sum_j P(i | j) \Delta O(j). \end{aligned} \quad (3)$$

Moving the blurred reference term to the left-hand side yields a formal structure analogous to Eq. (1); i.e., the blurred difference image is the convolution

$$\begin{aligned} \Delta I(i) &= I(i) - \sum_j P(i | j) O_{\text{REF}}(j) \\ &= \sum_j P(i | j) \Delta O(j), \end{aligned} \quad (4)$$

which allows us to use the RL formalism to deconvolve a solution for the unblurred difference, which can then be added to the unblurred reference to obtain the deconvolved complete image.

The effectiveness of this procedure in eliminating artifacts is illustrated in Fig. 7, where standard and differential deconvolutions are compared. Note the early appearance of a bright ring

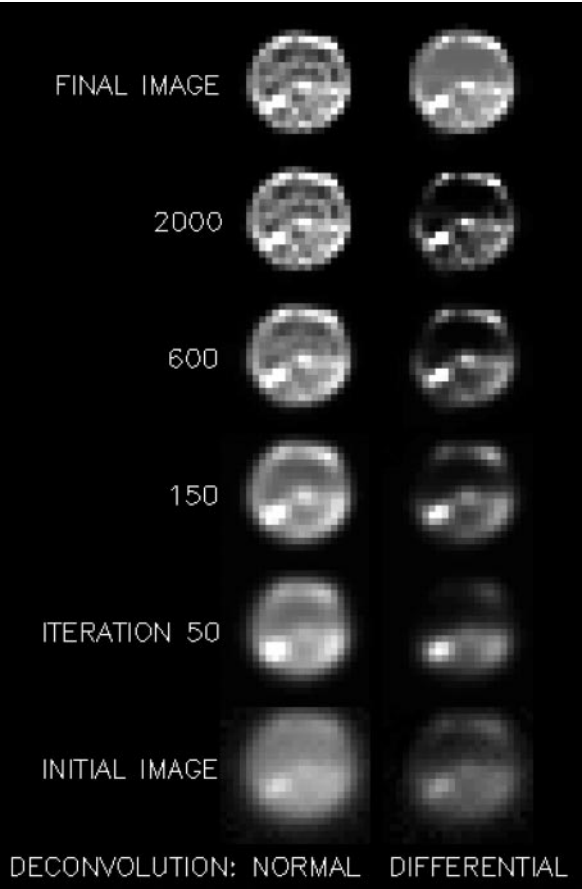


FIG. 7. Normal RL (left) and differential deconvolution (right) of a J-filtered NSFCAM image (nep0581), obtained on 13 August 1996 at 10:01 UT. The reference image for the differential deconvolution was a flat disk at 110 DN. The full image deconvolution and the difference image deconvolution are compared for unaccelerated iterations up to 2000. The final image (top row) for the differential deconvolution is the sum of the unblurred reference and the final deconvolved difference image.

at what appears to be the “limb” in the full image deconvolution. This is the first “ringing” artifact, which moves outward and narrows as new rings are formed at higher iteration numbers. This effect is completely absent in the differential deconvolution. Also note the absence of speckle artifacts in the final image obtained from adding the unblurred reference to the deconvolved difference. The full-image deconvolution is a blend of real features and artifacts that changes with iteration number in a nonconvergent manner, while the differential deconvolution converges to a well-defined final result.

In order for the differential deconvolution to be successful, it is necessary to know the location of Neptune to a small fraction of a pixel, so that the simulated reference image can be properly placed within the coarser image grid and create the correct limb brightness for each limb pixel. The appropriate DN level for the reference image is obtained by trial and error. We used the largest DN that did not yield negative DN values after subtraction of the blurred reference from the original image.

Previous application of the RL algorithm to deconvolution of groundbased Neptune images, e.g., by Heasley (1984) and Heasley *et al.* (1984), used far fewer iterations (6) and obtained far less spatial resolution in the final images (compare their Fig. 5 to our Fig. 3, which has dramatically more detail). Their results may have been limited by their approximation of the PSF as a two-dimensional Gaussian of fixed axis directions. Even when symmetric, the PSF would not be expected to follow a Gaussian shape except very near the core (see Appendix A of Paper II). More often, not only is the PSF not symmetric, it also has spatial structure that is impossible to adequately represent with such a simple two-dimensional Gaussian function. It is also important to use the PSF that records the exact seeing conditions that occurred during the exposure of the image to be deconvolved. Heasley *et al.* (1984) apparently fit their Gaussian function to stellar images, but they do not state whether the stellar image was in the same frame as Neptune. Thus their results might have been degraded further by seeing variations between PSF and planetary imaging.

Not only do we obtain far greater detail than Heasley *et al.* (1984), it is also the case that the detail has reality (besides the obvious consistency of features in the various images shown in Fig. 3, we also provide quantitative measures of consistency in Section 7.4).

7.4. Deconvolution Consistency for Successive Images

The combined performance of differential deconvolution and navigation can be assessed by comparing results applied to a sequence of images taken over a short enough time span that Neptune itself does not change significantly. In Fig. 8 we provide such a comparison for 15 J-filter images obtained over a 5-min time span, individually navigated and differentially deconvolved. The differences among deconvolved images of the same planetary configuration are a result of differences in seeing and the random differences associated with noise in the images. We defined four target boxes at fixed positions relative to our derived Neptune centers in the navigated images. For each target box we computed intergated and peak DN values, positions of the brightest pixel and the centroid, and standard deviations of each. The results, summarized in Table V, indicate a high degree of positional accuracy, with centroid standard deviations

TABLE V Consistency of Deconvolution of Successive J-Filter Images													
Box	X_{cnd}^a	SD^b	X_{max}^c	SD^b	Y_{cnd}^a	SD^b	Y_{max}^c	SD^b	ΣDN	SD	Max	SD	
1	10.9	0.1	10.9	0.2	11.3	0.1	11.5	0.5	2615	6%	604	19%	
2	11.4	0.2	11.4	0.6	20.9	0.1	20.9	0.3	461	20%	186	28%	
3	15.4	0.1	15.5	0.7	13.6	0.1	13.7	0.2	957	14%	298	22%	
4	19.3	0.1	19.4	0.7	20.2	0.1	20.2	0.5	1087	10%	425	22%	

^a Mean location of centroid in units of original image pixels.
^b Standard deviation in pixels.
^c Mean location of brightest pixel in units of original image pixels.

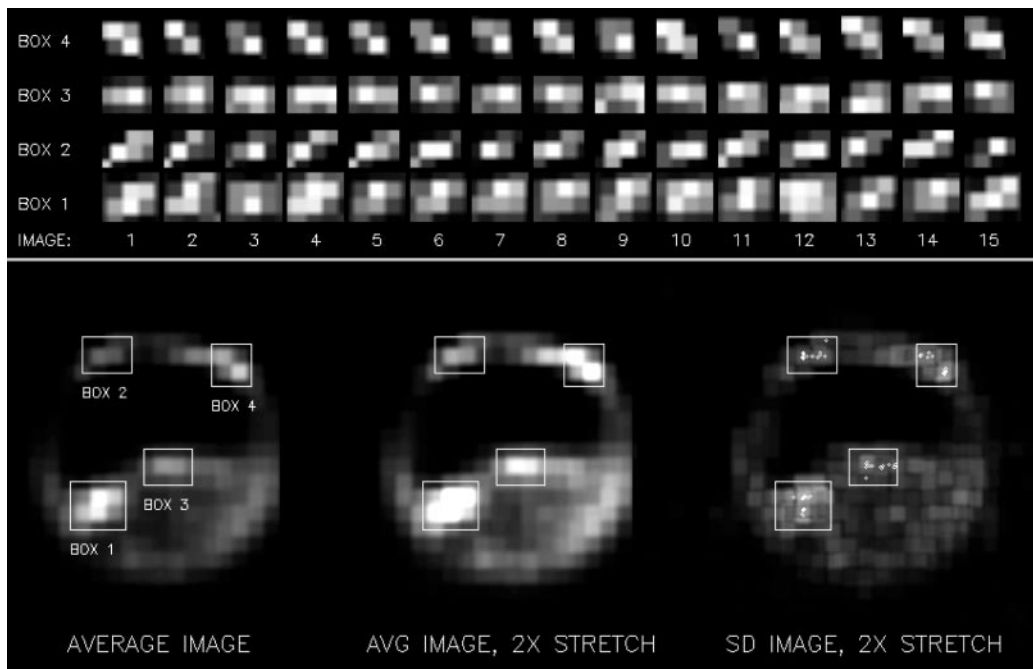


FIG. 8. Average (lower left and center) deconvolved images for 15 J-filter NSFCAM images obtained over a 5-min time interval. The rightmost image is the standard deviation of the 15 deconvolved images. Differential deconvolutions were used without pedestal add-back so that centroid computations would not be dominated by the pedestal contribution. Selected target boxes are outlined and numbered in the bottom panel, and individual image sections for all images are displayed in the top panel. The locations of the brightest pixel within the target boxes are plotted as bright points on the SD image. See text for discussion.

generally ~ 0.1 pixels. The location of the brightest pixels is much more variable showing SD values from 0.2 to 0.7 pixels in the x coordinate and 0.2–0.5 pixels in the y coordinate. The y coordinate is more stable because most of the cloud features have much larger contrast in that direction, and are more poorly localized in the x direction. The standard deviation of the integrated DN values are typically 10% of the mean value, and the standard deviation of the peak values within the target boxes are typically 20%. Had we restricted our sample to the images with the best seeing, there would have been even less variation.

8. COMPARISON OF IRTF AND HST IMAGING RESULTS

As noted in Table II, there are three orbits during which IRTF and HST images can be directly compared. However, good seeing at the IRTF was limited to the first two orbits, during which air-mass values were about 1.3–1.4. Within these orbits there are three nearly simultaneous comparisons that can be made. These are presented in Fig. 9 where the IRTF images are shown in deconvolved form to permit close comparison of cloud positions, which would not be possible in the raw images.

In the first row, IRTF 2.1- μm images numbered 371 and 372 are compared to an HST methane-band image made 3 min later. At 2.1 μm , sunlight is strongly absorbed by hydrogen gas in Neptune’s atmosphere, so that only high-altitude particulate scat-

tering yields any significant signal. The HST methane-band image also samples wavelengths at which Neptune’s atmosphere is strongly absorbing, but not so strongly as at 2.1 μm . The clouds seen at 30°N in all three images appear to reside at lower pressures than the clouds seen at 30° and 45°S , both of which appear relatively brighter in the 0.619- μm HST image than in the 2.1- μm IRTF image. These southern clouds may be more optically thick, but the northern clouds seem to extend to higher altitudes. Not surprisingly, the dimmer features in the IRTF images are not as well localized because they are more affected by noise. Note the 1-pixel difference in the longitudinal position of the small feature at 30°S .

The second row of images compares H-band IRTF images with an HST methane-band image taken only a few minutes later. Note that these images were made about 1.3 h after those in the first row, an interval corresponding to about 30° of planetary rotation. That rotation accounts for the decline in brightness of the most prominent feature between 30° and 45°N . These two H-band IRTF images have much higher signal/noise ratios than those in the first row and provide much better consistency in the distribution of cloud features. The third row of images compares two IRTF images made with the Spencer 1.7- μm filter with an F850LP HST image made at an intermediate time between the two IRTF images (and within 1.5 min of each). The Spencer 1.7- μm images provide the most precise location of the small cloud at 30°S .

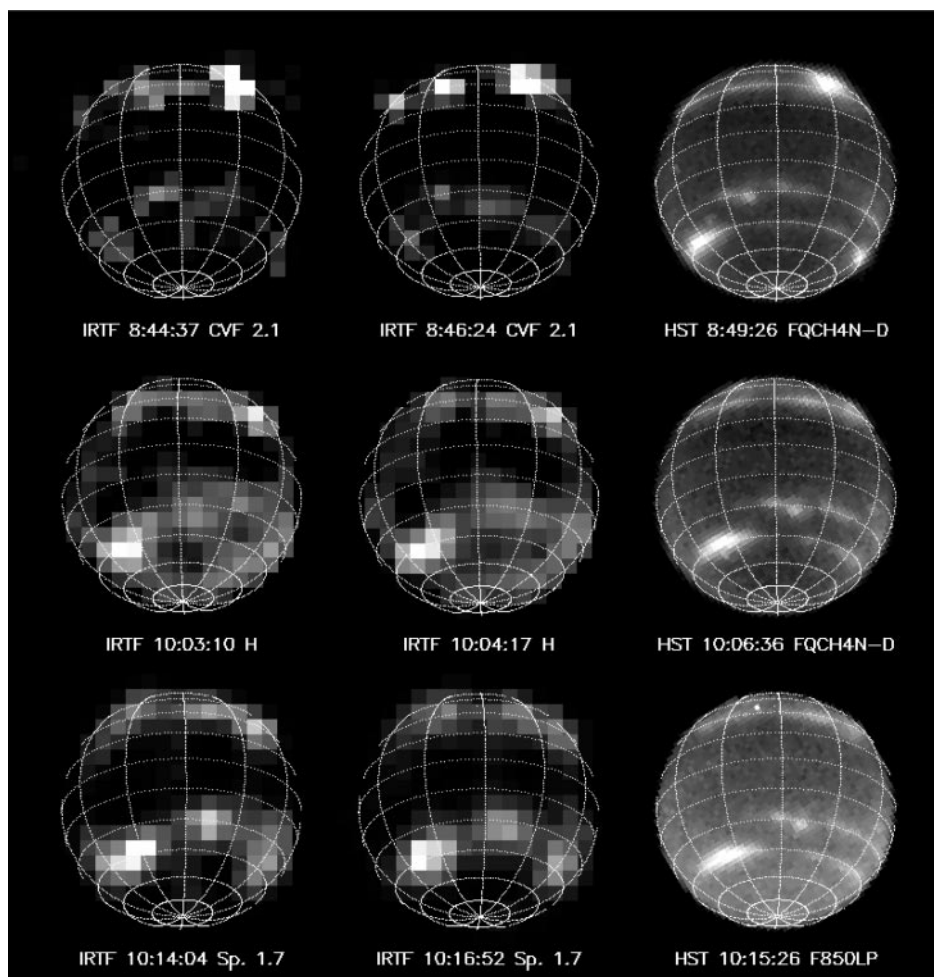


FIG. 9. Comparison of nearly simultaneous IRTF and HST images of Neptune on 13 August 1996. All grid lines are spaced at 30° in longitude and 15° in latitude. The sub-Earth latitude is 26°S . The HST FQCH4N-D filter is a narrow methane-band filter centered at 889.5 nm. The IRTF filters sample the $2.1\text{-}\mu\text{m}$ H_2 CIA absorption band (top row), and intermediate methane absorption bands at $1.4\text{--}1.8\text{ }\mu\text{m}$ (middle row), and $1.7\text{ }\mu\text{m}$ (bottom row). The IRTF images are shown in deconvolved form. All times are for the midpoint of the image exposures, not the usual exposure start times.

While these comparisons show relatively good agreement on the positions of cloud features between HST and IRTF results, the different morphologies that arise from different spectral sampling, and the image-to-image variations arising from noise, make it difficult to arrive at a solid quantitative comparison just on the basis of the relatively small sample of nearly simultaneous images. A much better statistical sample is provided by the cloud tracking results presented in Paper III. Three targets were sufficiently well defined in both HST and IRTF images to serve as useful targets for position comparisons: the bright companion feature (HST target 11), a small isolated cloud near 30°S (HST target 3), and two bright clouds near 45°S (HST targets 4 and 5), where the parenthetical target numbers are those used in Paper III. In Fig. 9, Target 11 can be seen at the upper right in the top row and Target 4 can be seen at the lower left in most of the images. Averaging IRTF latitude results over all filters yielded IRTF–HST differences of $-3.1 \pm 2.1^\circ$,

$-0.3 \pm 0.7^\circ$, and $-0.5 \pm 1.1^\circ$ (Paper III), which are all equivalent to a center-finding angular difference of $\sim 0.03''$ or ~ 0.2 IRTF pixels.

9. APPLICATIONS TO OTHER OBSERVING TARGETS

The offset navigation and deconvolution techniques that we used for Neptune can also be applied to other objects that have at least one small bright satellite that can be simultaneously imaged for use as a positional reference and PSF recorder. Uranus satisfies these requirements very well and offers advantages over Neptune in technique optimization because Ariel, its brightest satellite, is closer to the planet and has a smaller angular diameter ($0.084''$ at opposition vs $0.128''$ for Triton) and is only 1 mag dimmer than Triton. Uranus observations could thus use the NSFCAM $0.048''$ pixel scale, which would make possible retrieval of finer details. Because Uranus has

strong and asymmetric limb darkening at many wavelengths as well as ring light contamination, finding the center of Uranus by limb fitting is somewhat challenging. Thus the offset navigation has high utility for Uranus. Uranus is also a good target for differential deconvolution, although the reference synthetic image needs to be more complex than a flat disk, to account for latitudinal and center-to-limb variations. Successful application of differential deconvolution to groundbased IRTF images of Uranus at $1.7\ \mu\text{m}$, for which Uranus has a significant limb brightening, was recently reported by Sromovsky *et al.* (2000).

10. SUMMARY AND CONCLUSIONS

Coordinated observations of Neptune with the HST WFPC2 CCD camera and the IRTF NSFCAM InSb camera were obtained on 13–14 August 1996, with the objectives of constraining cloud structure, evolution, and motions. The 1996 HST provided a unique dense sampling of one rotation of Neptune at high spatial resolution, and with a wide variety of bandpass filters from UV to $1\ \mu\text{m}$, while the IRTF imaging provided unique spectral coverage at near-IR wavelengths from 1.1 to $2.4\ \mu\text{m}$ that provides better constraints on the upper tropospheric cloud structure. To relate these two data sets to best advantage we needed to improve the spatial resolution of the IRTF images using deconvolution, and carry out precise navigation of both data sets. Using a new limb-fitting method of HST image navigation and a refined limb-independent offset navigation of IRTF images, we achieved center-finding accuracy of $0.003''$ (0.05 pixels) for HST navigations and $0.03''$ (0.2 pixels) for IRTF navigations. The HST navigations were effective at avoiding problems due to limb distortions by bright cloud features. The IRTF navigations used offsets from Triton to locate Neptune's center, a procedure that was successful only after making precise determinations of the filter-dependent image scale of the NSFCAM instrument and determining its distortion characteristics for the first time. The benefits of improved navigational accuracy are the better collocation of data from different instruments and observatories, better determination of emission and viewing for radiation transfer modeling of vertical cloud structure, improved wind speed accuracy for a given observation time, and the capability to apply differential deconvolution.

Deconvolution of the groundbased images was essential for accurate location of cloud features, and for improved determination of spatially resolved I/F values. We developed a new technique, which we call differential deconvolution, that avoids ringing and speckling artifacts that normally limit the number of useful iterations that can be applied to planetary image deconvolutions. This subtracts a convolved model of the planetary disk before deconvolution then adds it back afterward, thus avoiding the problems associated with offsets and sharp edges. Based on star image measurements, we found that deconvolutions improved effective seeing by about a factor of 3, from initial values of $0.75''$ – $0.52''$ to about $0.25''$ – $0.152''$, respectively.

Our deconvolved images are the most detailed groundbased images of Neptune yet obtained without adaptive optics or speckle imaging. We obtained photometric consistency in the range of 10–20%, and geometric centroid position accuracy within a fixed box of better than 0.1 pixels, although the pixels of maximum brightness varied in position by 0.2–0.5 pixels in the direction of maximum contrast gradient.

As well as providing complementary wavelength coverage, the higher resolution of the HST observations provide a verification test for our groundbased navigation and deconvolution methods. These navigation and deconvolution techniques are applied to circulation measurements and the analysis of discrete feature vertical haze/cloud structure in Paper III.

APPENDIX A

Correction of NSFCAM Image Distortions

Methods. Because our method of navigating IRTF images of Neptune requires precise offsets from Triton, we found it necessary to determine and correct for NSFCAM image distortions. We were able to address this issue using the 14 August 96 data set containing multiple star images and image pairs offset by $\sim 10''$. Because a pointing change of $10''$ moves the stars to substantially different locations on the array, image distortions are revealed by changes in stellar angular separations with pointing direction. We assumed that corrected coordinates (x', y') could be written as

$$(x', y') = (x_o, y_o) + (x - x_o, y - y_o)(1 + k(r/r_r)^2), \quad (5)$$

where (x, y) are the raw coordinates, (x_o, y_o) is the center of distortion (near the center of the image), $r^2 = (x - x_o)^2 + (y - y_o)^2$, and $r_r = 127$ pixels. This provides a radially directed correction that increases quadratically with distance from the center, with proportionality constant k . This is consistent with the classical form of distortion derived in third-order aberration theory (Born and Wolf 1980), for which the aberration itself (difference between ideal and actual image coordinates) is proportional to the cube of the off-axis distance. To determine the coefficient k and the effective central coordinates (x_o, y_o) , we selected those values that minimize $\chi^2 = \chi_x^2 + \chi_y^2$, where

$$\chi_x^2 = \sum_{i=1}^N (dx_a(i, k) - dx_b(i, k))^2 / (\sigma_{x,a}^2 + \sigma_{x,b}^2), \quad (6)$$

in which $dx_a(i, k)$ and $dx_b(i, k)$ are x components of the vector connecting the i th star pair in beam positions a and b respectively, and $\sigma_{x,a}$ and $\sigma_{x,b}$ are the uncertainties in those components. Analogous definitions apply to the y component.

Results for the J filter. Using 17 quartets of measurements on 17 star pairs in two different beam positions, we found best-fit parameter values of $k = 0.0055 \pm \begin{smallmatrix} 0.0006 \\ 0.0008 \end{smallmatrix}$, $x_o = 137.5 \pm \begin{smallmatrix} 3.3 \\ 3.9 \end{smallmatrix}$, and $y_o = 138.2 \pm \begin{smallmatrix} 4.3 \\ 2.1 \end{smallmatrix}$. The corrected coordinates yield a factor of 6 reduction in χ^2 and nearly factor of 3 reduction in the standard deviation of differences from the desired zero value. The χ^2 minimum value is about 3–5 times N , indicating that the total noise in the measurements is a factor 1.7–2.2 greater than indicated by our uncertainty estimates. The residual variation, though rather small, is on the order of 0.1 pixels, and represents one of the larger contributors to the error budget in our offset navigation method. The sign of k being positive means that the NSFCAM image has a barrel distortion, so that features at the edge of the frame appear too close to the center of the frame.

In order to use this correction, we first locate Triton in an image. Next we correct the coordinates to values that would apply to an undistorted image. Using the image orientation and ephemeris values for the angular offsets between Triton

and Neptune at the central time of the image, we divide by the central image scale to determine the corrected pixel offset, and add that to the Triton coordinates to obtain the corrected position of Neptune's center in an undistorted image. These coordinates are then distorted by the inverse of the correction function to define the position of Neptune's center in the distorted image.

The local image scale in the distorted NSFCAM image varies with position. It is smallest near the center and increases toward the edge; i.e., there are more arcseconds per pixel at the edges of the image. The radial scale is given by $S_o(1 + 3k(r/r_c)^2)$ and the tangential scale by $S_o(1 + k(r/r_c)^2)$, where S_o is the filter-dependent adopted central scale at (x_o, y_o) , in arcseconds/pixel as given in Table IV. To preserve proper angular area, we use the geometric mean scale, which is approximated by $S(r) = S_o(1 + 2k(r/r_c)^2)$. At $r = 127$ pixels, this evaluates to $S(r)/S_o = 1.01$, while at a more typical distance of 60 pixels, the effect is less than 0.25%. In any case, the local scale is taken into account in transforming image coordinates to planetary coordinates.

Wavelength dependence. IRTF images of Neptune and Triton obtained in August 1998 (Sromovsky *et al.* 1998) provide suitable data for investigating whether the NSFCAM distortion has a wavelength dependence. These data consisted of a-b pairs in each of the broadband filters. The images for each pair were exposed in succession with the telescope aim points differing by 15'' and with the second image placing Triton near the corner of the image frame where significant distortion is present. To measure the effect of the distortion we first determined Neptune's center by offsetting from Triton as described for the 1996 observations, except that we ignored distortion corrections. We then extracted 9X blow-ups centered on these derived positions. Were no distortion present, these blow-ups for a and b images would be aligned, but because distortion was present, the features in these image pairs were offset from each other by about 0.4 pixels in the y direction and 0.3 pixels in the x direction, which we measured using cross-correlation. In Fig. 10 these measurements are compared with the offsets computed using the model we developed from the J-filter star-pair analysis, which shows that the distortion does not have a large wavelength dependence, and is further evidence that the distortion is characterized well enough to establish image centers to within about 0.1 pixels.

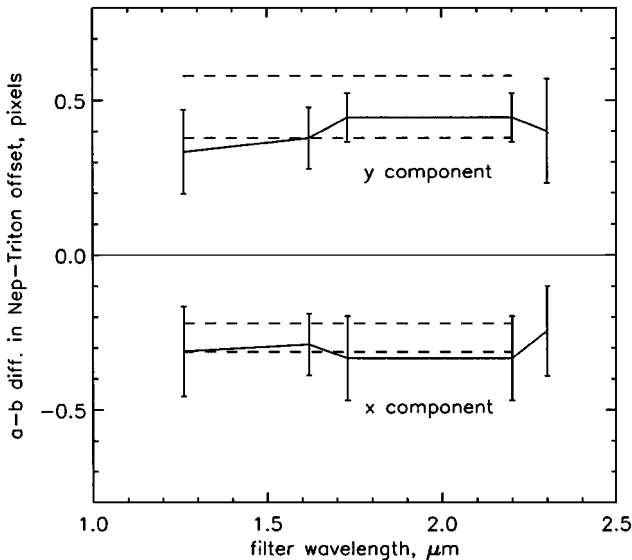


FIG. 10. Neptune-Triton a-b offset differences (points with error bars), as measured by cross-correlation of features in uncorrected images, compared to offsets predicted using distortion coefficients given in the text (shown as dashed lines at $\pm 1\sigma$ uncertainty bounds). Image data used in this analysis were obtained in August 1998.

APPENDIX B

Validation of Uncertainty Estimates

Uncertainty in Position Measurements in IRTF Images

To estimate uncertainty in position measurements of point sources from the signal and noise characteristics of the images in which they are measured, we developed an empirical model based on Monte Carlo simulations. We started with a noise model for the images. Denoting $\langle DN \rangle$ as the average DN for a single exposure, we computed its expected uncertainty

$$\sigma_{(DN)} = \left(\frac{\langle DN \rangle}{10N_C} + \frac{5.5^2}{N_C N_R} \right)^{1/2},$$

where N_R is the number of nondestructive reads, N_C is the number of repeated exposures that are coadded, and the expected noise per read of 5.5 DN (55 electrons) is based on measurements of a comparable array (Greene and Denault 1994). To this we added 2% of amplitude noise to simulate flat field correction errors. We computed a symmetric Gaussian of FWHM equal to 3 pixels to simulate the star image, and added a one-dimensional smear to simulate asymmetric seeing distortions. The empirical model that fit our Monte Carlo simulations reasonably well is $\sigma_{pos} = A^{1/2} * [0.0085 + 2.7(DN_{pk}(N_{coadd}/40)^{1/2})^{-1.4}]$, where $A = \max(FWHM_x, FWHM_y) / \min(FWHM_x, FWHM_y)$ is a factor that attempts to capture the effect of fitting a Gaussian to a PSF that does not really have a Gaussian shape. The deviation from symmetry of the Gaussian fit, as indicated by the ratio FWHM fit values for x and y directions, is used to scale the positional error estimate.

The validity of this model applied to real observations was tested by making measurements of stars in pairs of images for which exposure, filter, and beam position were identical, then computing star-to-star distances and estimated distance errors for each member of the pair, and comparing those predictions to the observed distance difference between the two members of the pair. For a good model, we would expect to find that the observed distance differences, divided by our computed uncertainty estimate, and averaged over an infinite number of cases, would have a mean value of 0 and a standard deviation of unity. For a set of 60 samples, with coadd numbers of either 40 or 10, and DN peaks between about 10 and 1000, we found this ratio to have a standard deviation of 0.96, validating the model to more than adequate precision.

Uncertainty in Finding Neptune's Center in HST Images

As an independent test of center-finding accuracy, we measured Triton's position in the 1994 HST images, corrected the positions for distortions following the equations given in the WFPC2 Instrument Manual (Biretta *et al.* 1996), computed the distances between Triton and Neptune's center, and finally divided those corrected pixel distances into the corresponding distances in arcseconds obtained from ephemeris computations. This ratio of angular distance to corrected pixel distance should equal the HST pixel scale, and its variation should be an indication of the center-finding error for Neptune. Over a typical Neptune-Triton separation distance of 16'' (351 WFPC2 pixels), an error of 0.1 pixels leads to a scale uncertainty of 0.028%, which is slightly larger than the 0.02% uncertainty in the HST pixel scale. Thus, this comparison is a relatively sensitive check on the center-finding measurements. The 1σ ephemeris error for the Neptune-Triton radial distance is only 13 km (Jacobson *et al.* 1991), which is less than 1 milliarcsecond and thus completely insignificant (although we have seen up to 10-milliarcsecond discrepancies in offsets computed from RA and Dec values and direct Horizon outputs).

Our distance comparisons in Fig. 11 clearly show that our Neptune center-finding results are very consistent with the HST image scale of $0.04554 \pm 0.00001''/\text{pixel}$, implying a center-finding consistency of better than 0.1 WFPC2 pixels (better than 4.5 milliarcseconds).

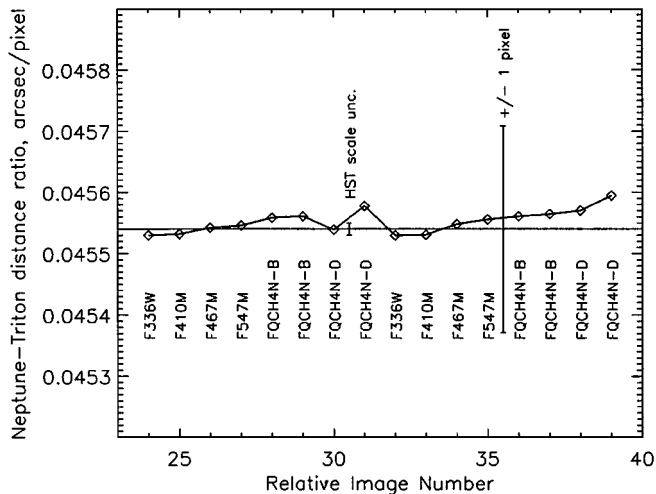


FIG. 11. Comparison of image scales inferred from the ratio of the ephemeris angular separation of Neptune and Triton to the center-to-center difference measured in HST WFPC2 images, with coordinates corrected for distortion. These results are from 18–19 Oct 1994 images, for which Triton is most distant from the edge of the image, and thus provide the most valid comparisons.

ACKNOWLEDGMENTS

This work is based on observations with the NASA/ESA Hubble Space Telescope, obtained at the Space Telescope Science Institute, which is operated by the Association of Universities for Research in Astronomy, Inc., under NASA Contract NAS5-26555. We thank Support Astronomer Keith Noll and Program Coordinator Denise Taylor, who provided excellent assistance in designing the HST observing sequence. We also made use of observations obtained at the NASA Infrared Telescope Facility, operated for NASA by University of Hawaii Institute for Astronomy. Support for this work was provided by NASA through Space Telescope Science Institute Grants AR-06374.01-95A and GO-06650.01-95A, and through the Planetary Astronomy Program, under Grant NAG5-6788, and Visiting Astronomer support by the IRTF. We are grateful for the excellent support provided by IRTF astronomer Bob Greene and telescope operator Lars Berkgut, and to IRTF director Bob Joseph for his efforts in arranging the observing schedule to coincide with the HST observations. We thank Heidi Hammel and an anonymous reviewer for extensive and helpful comments.

REFERENCES

- Acton, C. H. 1996. Ancillary data services of NASA's navigation and ancillary information facility. *Planet. Space Sci.* **44**, 65–70.
- Allen, C. W. 1964. *Astrophysical Quantities*, 2nd ed. Oxford Univ. Press, New York.
- Baines, K. H., and H. B. Hammel 1994. Clouds, hazes, and the stratospheric methane abundance in Neptune. *Icarus* **109**, 20–39.
- Baines, K. H., and W. H. Smith 1990. The atmospheric structure and dynamical properties of Neptune derived from ground-based and IUE spectrophotometry. *Icarus* **85**, 65–108.
- Baines, K. H., P. A. Yanamandra-Fisher, L. A. Lebofsky, T. W. Momary, W. Golish, C. Kaminski, and W. J. Wild 1998. Near-infrared absolute photometric imaging of the uranian system. *Icarus* **132**, 266–284.
- Biretta, J. A., C. Burrows, J. Holtzman, I. Heyer, M. Stevens, S. Baggett, S. Casertano, M. Clampin, A. Fruchter, H. Ferguson, R. Gilliland, R. Griffiths, J. Krist, K. Noll, C. O'Dea, M. Stiavelli, A. Suchkov, J. Surdej, and B. Whitmore 1996. *WFPC2 Instrument Handbook*, Version 4.0. Baltimore, STScI.
- Born, M., and E. Wolf 1980. *Principles of Optics*, 6th ed. Pergamon Press, Oxford.
- Caldwell, J., T. Owen, A. R. Rivolo, V. Moore, G. E. Hunt, and P. S. Butterworth 1981. Observations of Uranus, Neptune, and Titan by the International Ultraviolet Explorer. *Astron. J.* **86**, 298–305.
- Crisp, D., J. Trauger, K. Stapelfeldt, T. Brooke, J. Clarke, G. Ballester, R. Evans, and the WFPC2 Science Team 1994. Hubble Space Telescope wide field planetary camera 2 observations of Neptune. *Bull. Am. Astron. Soc.* **26**, 1093.
- Davies, M., V. K. Abalakin, A. Brahic, M. Bursa, B. H. Chovitz, J. K. H. Lieske, P. K. Seidelmann, A. T. Sinclair, and I. S. Tiufin 1992. Report of the IAU/IAG/COSPAR Working Group on cartographic coordinates and rotational elements of the planets and satellites—1991. *Celest. Mech. Dynam. Astron.* **53**, 377–397.
- Fink, U., and S. Larson 1979. The infrared spectra of Uranus, Neptune, and Titan from 0.8 to 2.5 microns. *Astrophys. J.* **233**, 1021–1040.
- Giorgini, J. D., D. K. Yeomans, A. B. Chamberlin, P. W. Chodas, R. A. Jacobson, M. S. Keesey, J. H. Lieske, S. J. Ostro, E. M. Standish, and R. N. Wimerly 1998. *Horizons, JPL's On-Line Solar System Data and Ephemeris Computation Service*, a user's guide available from ftp://ssd.jpl.nasa.gov/pub/ssd/Horizons_doc.ps.
- Greene, T., and A. Denault 1994. *CSHELL: NASA IRTF Cryogenic Echelle Spectrograph User's Manual*, Rev. 2.0.1. Institute for Astronomy, University of Hawaii, Honolulu, HI.
- Hammel, H. B., and G. W. Lockwood 1997. Atmospheric structure of Neptune in 1994, 1995, and 1996: HST imaging at multiple wavelengths. *Icarus* **129**, 466–481.
- Hammel, H. B., K. H. Baines, and J. T. Bergstralh 1989. Vertical aerosol structure of Neptune: Constraints from center-to-limb profiles. *Icarus* **80**, 416–438.
- Hammel, H. B., G. W. Lockwood, J. R. Mills, and C. D. Barnet 1995. Hubble Space Telescope imaging of Neptune's cloud structure in 1994. *Science* **268**, 1740–1742.
- Heasley, J. N. 1984. Numerical restoration of astronomical images. *Pub. Astron. Soc. Pacific* **96**, 767–772.
- Heasley, J. N., C. B. Pilcher, R. R. Howell, and J. J. Caldwell 1984. Restored methane band images of Uranus and Neptune. *Icarus* **57**, 432–442.
- Jacobson, R. A., J. E. Reidl, and A. H. Taylor 1991. The orbits of Triton and Nereid from spacecraft and Earthbased observations. *Astron. Astrophys.* **247**, 565–575.
- Karkoschka, E. 1994. Spectrophotometry of the jovian planets and Titan at 300- to 1000-nm wavelength: The methane spectrum. *Icarus* **111**, 174–192.
- Legget, S., and T. Denault 1996. *NSFCAM 256 × 256 InSb Infrared Array Camera User's Guide*, Version 3. NASA Infrared Telescope Facility.
- Lucy, L. B. 1974. An iterative technique for the rectification of observed distributions. *Astrophys. J.* **79**, 745.
- Neff, J. S., T. A. Ellis, J. Apt, and J. T. Bergstralh 1985. Bolometric albedos of Titan, Uranus, and Neptune. *Icarus* **62**, 425–432.
- Neff, J. S., D. C. Humm, and J. T. Bergstralh 1984. Absolute spectrophotometry of Titan, Uranus, and Neptune: 3500–10,500 Å. *Icarus* **60**, 221–235.
- Richardson, B. H. 1972. Bayesian-based iterative method of image restoration. *J. Opt. Soc. Am. A* **62**, 55–59.
- Smith, B. A., and H. J. Reitsema 1982. Imaging of Uranus and Neptune. In *Uranus and the Outer Planets, Proceedings of IAU/RAS Colloq. No. 60* (G. Hunt, Ed.), pp. 173–179. Cambridge Univ. Press, London.
- Smith, B. A., L. A. Soderblom, D. Banfield, C. Barnet, A. T. Basilevsky, R. F. Beebe, K. Bollinger, J. M. Boyce, A. Brahic, G. A. Briggs, R. H. Brown, C. Chyba, S. A. Collins, T. Colvin, A. F. Cook II, D. Crisp, S. K. Croft, D. Cruikshank, J. N. Cuzzi, G. E. Danielson, M. E. Davies, E. DeJong, L. Dones, D. Godfrey, J. Gougen, J. Grenier, V. R. Haemmerle, H. Hammel, C. J. Hansen, C. P. Helfenstein, C. Howell, G. E. Hunt, A. P. Ingersoll,

- T. V. Johnson, J. Kargel, R. Kirk, D. I. Kuehn, S. Limaye, H. Masursky, A. McEwen, D. Morrison, T. Owen, W. Owen, J. B. Pollack, C. C. Porco, K. Rages, P. Rogers, D. Rudy, C. Sagan, J. Schwartz, E. M. Shoemaker, M. Showalter, B. Sicardy, D. Simonelli, J. Spencer, L. A. Sromovsky, C. Stoker, R. G. Strom, V. E. Suomi, S. P. Synnot, R. J. Terrile, P. Thomas, W. R. Thompson, A. Verbiscer, and J. Veverka 1989. Voyager 2 at Neptune: Imaging science results. *Science* **246**, 1422–1454.
- STSI 1998. Space Telescope Science Data Analysis System, Version 2.0.1, February 9, 1998. Space Telescope Science Institute, Baltimore, Maryland.
- Sromovsky, L. A., P. M. Fry, S. S. Limaye, K. H. Baines, and T. Dowling 1998. HST and IRTF observations of Neptune during 1998. *Bull. Am. Astron. Soc.* **30**, 1098.
- Sromovsky, L. A., P. M. Fry, K. H. Baines, and T. Dowling 2001a. Coordinated 1996 HST and IRTF observations of Neptune and Triton. II. Implications of disk-integrated photometry. *Icarus* **149**, 000–000.
- Sromovsky, L. A., P. M. Fry, T. Dowling, K. H. Baines, and S. S. Limaye 2001b. Coordinated 1996 HST and IRTF Observations of Neptune and Triton. III. Neptune's atmospheric circulation and cloud structure. *Icarus* **149**, 000–000.
- Sromovsky, L. A., J. R. Spencer, K. H. Baines, and P. M. Fry 2000. Ground-based observations of cloud features on Uranus. *Icarus* **146**, 307–311.
- Voit, M. 1997. *HST Data Handbook, Vol. 1, Current Instruments*. Space Telescope Science Institute, Baltimore, MD.
- Warwick J. W., D. R. Evans, G. R. Peltzer, R. G. Peltzer, J. H. Romig, C. B. Sawyer, A. C. Riddle, A. E. Schweitzer, M. D. Desch, M. L. Kaiser, W. M. Farrell, T. D. Carr, I. de Pater, D. H. Staelin, S. Gulkis, R. L. Poynter, A. Boischot, F. Genova, Y. LeBlanc, A. Lecacheux, B. M. Pedersen, and P. Zarka 1989. Voyager planetary radio astronomy at Neptune. *Science* **246**, 1498–1501.
- White, R. L. 1993. Improvements to the Richardson–Lucy method. *Image Restoration Newsletter* No. 1, pp. 11–22, Space Telescope Science Institute, Baltimore, MD.